Chemical Engineering & Processing: Process Intensification 198 (2024) 109728

Contents lists available at ScienceDirect

Chemical Engineering and Processing - Process Intensification

journal homepage: www.elsevier.com/locate/cep

Dynamic modeling and robust optimal operation of the hydrothermal synthesis of zeolites in a continuous oscillatory baffled reactor

Robin Semrau [a,*], Heidy Ramirez Mendoza [b], Cécile Lutz [b], Sebastian Engell [a]

[a] TU Dortmund, Process Dynamics and Operations Group, Emil Figge Straße 70, Dortmund, 44227, NRW, Germany
[b] ARKEMA, Service Adsorption, Groupement de Recherche de Lacq, BP 34, Lacq, 64170, France

ARTICLE INFO

Keywords:
Zeolite production
Process intensification
Oscillatory baffled reactor
Rigorous model
Optimal operation
Optimization under model uncertainty

ABSTRACT

Continuous flow synthesis offers major advantages in the production of specialty products, e.g. zeolites, such as tight temperature control and lower variation in product quality. Here we consider the hydrothermal synthesis of NaX zeolites in a continuous oscillatory baffled reactor (COBR). A process model is derived from physico-chemical relationships to analyze and optimize the operation of a pilot scale continuous oscillatory baffled reactor for zeolite synthesis. The process model is validated using plant data. Furthermore, the uncertainty of the model predictions is quantified. Based on this analysis, robust optimization is used to compute robust optimal operation points of the COBR. These optimal operation points are validated by the application to a real pilot plant.

1. Introduction

Zeolites are an important class of ceramics for industrial and consumer applications. The production of zeolites is often performed by hydrothermal synthesis which requires long residence times at elevated temperatures [1]. In industrial scale, it is usually performed in large batch reactors [2,3]. However, continuous flow synthesis offers great advantages over batch production, such as lower energy demand caused by better heat integration, lower product variations, and smaller equipment [4–6]. Therefore, the continuous production of zeolites is a current field of intense research [5,7]. The semi-continuous synthesis of zeolites was first studied by Cundy et al. [8]. A disadvantage of continuous stirred tank reactors is that they decrease the product quality due to high back mixing. Therefore, they are only applicable for synthesizing low-quality zeolites [2]. Zeolite synthesis in tubular reactors has been studied for different products by Liu et al. [9] and Vandermeersch et al. [10]. However, these works include a speedup of the reactions by changing the synthesis conditions to be able to finish the process within short residence times, which is only applicable to selected zeolites. Only residence times up to several minutes were realized because of the necessary flow velocities.

Continuous oscillatory baffled reactors are promising candidates for reaction and crystallization processes that involve slurries. The improved mixing and heat transfer characteristics of the COBR were shown e.g., by Mackley and Ni [11] and Mackley and Stonestreet [12]. The COBR technology has already been applied to different problems such as the continuous crystallization of pharmaceuticals [13], the solution crystallization of l-glutamic acid [14], or the production of biofuel [15]. The idea to utilize the advantages of the continuous oscillatory baffled reactor for zeolite synthesis has first been reported by Nicolas et al. [16]. Recently, Ramire. Mendoza et al. [17] demonstrated the efficient production of zeolite NaX in a pilot scale continuous oscillatory baffled reactor over several hours of production. The COBR provides a tight residence time distribution with an intense radial mixing to prevent sedimentation of the zeolite suspension and clogging of the reactor.

The crystallization of zeolites has been studied intensely. Various crystallization models have been proposed to describe the observed phenomena. However, most of these models were formulated for batch processing and describe the crystallization process as a time-dependent process with an analytic expression for the crystallinity [18], such as the well-known Avrami [19] model which describes the crystallization as a function of reaction time for a random distribution of nuclei or the model proposed by Gualtieri [20] that models the nucleation probability as a function of reaction time. However, these models are not suitable for the description of spatially distributed and continuous processes. Population balance models offer a higher potential for integration in a process model for a continuous plant. Thompson and Dyer [21] developed a population balance model for the crystallization reaction, Nikolakis et al. [22] included the effect of the gel microstructure into the description of the nucleation step. Our model for a continuous production of zeolites in a tubular reactor is based on the proposed

* Corresponding author.
E-mail address: Robin.Semrau@tu-dortmund.de (R. Semrau).

https://doi.org/10.1016/j.cep.2024.109728
Received 4 December 2023; Received in revised form 3 February 2024; Accepted 28 February 2024
Available online 1 March 2024

population balance models of the zeolite kinetics which is integrated into the energy and material balances along the reactor.

When process models are used for process design, operation and control the discrepancies between the predictions of the model and the real behavior of the process have to be taken into account in order to achieve the specifications of the process also in the presence of these deviations, that are generally termed "plant-model mismatch". Optimal design and operation in the presence of plant-model mismatch belongs to the domain of optimization under uncertainty which is a broad and active field of research. Dependent on the formulation of the optimization problem and the assumptions about the uncertainty, a variety of different approaches exist. In this work, the focus is on constraint satisfaction in the presence of parametric uncertainties, i.e. errors in the assumed values of the model parameters. Classical robust approaches handle such problems by the formulation of a min–max problem [23] where the specifications must be met for the worst case values of the uncertain parameters. This however, can lead to very conservative results. In probabilistic approaches, this is circumvented by formulating chance constraints, i.e. the constraints have to be satisfied with a prescribed probability. To solve such optimization problems involves the approximation of the probability distribution of the constraint functions [24] which is difficult for nonlinear dynamic process models. In this work, the unscented transform [25] is used to approximate the probability distribution with low computational effort, similar to [26].

Semrau and Engell [27] presented simulation studies of the flexible, dynamic operation of continuous zeolite production in an oscillatory baffled reactor for a fluctuating price of electrical energy. The operating parameters (throughput, inputs of heating power) were optimized to minimize the production cost over an interval of e.g. one day for time-varying prices of electric energy while meeting the specification of the quality of the product. To realize such a demand response strategy at a real plant, robust operating parameters must be determined that lead to the satisfaction of the specification of the product properties also in the case of model errors.

Therefore, in this work, the robust operation of the synthesis of zeolite NaX (FAU type) in a pilot scale COBR is investigated. A mathematical process model consisting of partial differential equations of the zeolite production process, based on rigorous sub-models is presented first. The mass transfer and the energy transfer models and the resulting prediction of the crystallization of the zeolite are validated separately on the basis of experimental data. The plant model mismatch is analyzed and described by a covariance matrix of the uncertainty of selected parameters. Based on the unscented transform, a robust optimization of the operating points is performed and the validity of computed operating points is verified by the application to the pilot scale production plant.

2. Process

The scheme of the pilot-scale zeolite production process is shown in Fig. 1. This work considers the continuous hydrothermal production of zeolite X (FAU-type structure) from sodium silicate, aluminum oxide, and sodium hydroxide. The alkaline alumina and silica solutions are prepared separately and provided via the two feeding tanks. The reactants are pumped by two gear pumps into the high shear inline mixer along with a fixed amount of seed crystals. The addition of seeds to the reactive mixture prevents the necessity of an aging step in the zeolite formation and promotes the formation of the desired crystalline phase. The reaction mixture is subsequently fed into the continuous oscillatory baffled reactor (COBR). The COBR has a diameter of 43 mm and a total length of 42.4 m. The oscillations in a frequency range of 0.1–3 Hz and with amplitudes of 10–150 mm are imposed by two gear pumps. The COBR pipe is surrounded by a heating jacket which is operated in a co-current flow configuration with thermal oil as heating medium. The COBR is equipped with three heating jackets along the reactor length. These are coupled to thermostatic baths that are operated at variable set-points. The throughput of the zeolite suspension is between 34.2 kg/h and 91.2 kg/h. The temperature has to be lower than 130 °C to prevent the formation of gas bubbles and the formation of undesired zeolite phases, especially zeolite-A or zeolite-Y [28]. The temperature profile of the reaction medium is measured by 11 thermocouples that are uniformly distributed over the reactor length. The reactor is equipped with five sampling points along the length of the reactor to take samples for off-line analysis of the reactive suspension. For detailed information about the experimental set-up, the operation procedure, the involved zeolite chemistry and the analytics we refer the reader to the prior work by Ramire Mendoza [29] and Ramire. Mendoza et al. [17].

3. Dynamic model

3.1. Mass transport

The behavior of the oscillatory baffled reactor is described by a rigorous dynamic model. The content of the tubular reactor is assumed to be spatially inhomogeneous in the axial domain with the reactor length L. The radial variation of concentrations and temperatures are assumed to be small due to efficient mixing caused by the secondary vortices which are formed by the oscillating flow in the baffled tube [30]. The axial dispersion model is used to describe the back mixing caused by the flow patterns in the oscillatory baffled reactor. The general formulation of a standard axial dispersion model of a concentration $C_j(t,z)$ in the axial domain z with mixed boundary conditions at the inlet and a zero gradient condition at the outlet is given in Eq. (1).

$$\partial_t C_j(t,z) = -v\partial_z C_j(t,z) + D_{ax}\partial_z^2 C_j(t,z) + \kappa_j(t,z) \tag{1a}$$

$$0 = vC_{j,in} - vC_j(\cdot,0) + D_{ax}\partial_z C_j\Big|_{z=0} \tag{1b}$$

$$0 = \partial_z C_j\Big|_{z=L} \tag{1c}$$

$$C_j(0,\cdot) = C_{j,0} \tag{1d}$$

C_j are the different concentrations, e.g. of amorphous solid C_{am}. v is the velocity, and D_{ax} is the axial dispersion coefficient. These parameters (v, D_{ax}) are assumed to be constant over the reactor length. κ_j is the volumetric generation/consumption term of the species j e.g. of the amorphous solid κ_{am}, these are explained in detail in Section 3.3. The ratio of convection and dispersion in real reactors can be described using the Peclet number

$$Pe = \frac{vL}{D_{ax}}. \tag{2}$$

For high values of the Peclet number ($Pe > 100$) [31] the reactor dynamics are close to the behaving of a plug flow reactor.

3.2. Energy transport

The energy balance equations are formulated for three compartments, the reaction medium, the heating jacket, and the reactor walls. The energy transport of the reaction medium T_R in the reactor is described by Eq. (3). Only convective heat transport along the reactor length is considered. The specific heat of the zeolite crystallization is −2.38 kJ/mol [32] and the resulting adiabatic temperature rise is below 0.2 K. Therefore, the heat of reaction can be neglected. The inlet temperature of the reactor is considered via the inlet boundary condition (3c). The model includes the heat exchange with the reactor wall which is modeled separately.

$$\partial_t T_R(t,z) = -v\partial_z T_R(t,z)$$

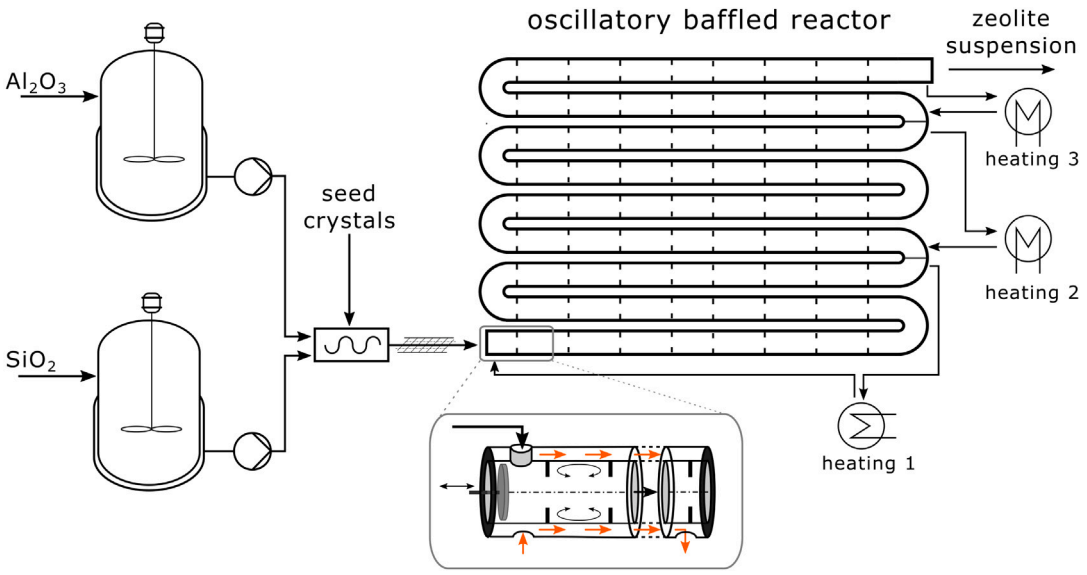

Fig. 1. Process flow diagram of the continuous oscillatory reactor set-up for the continuous zeolite production.

$$+ \frac{kA_{R,w}}{\rho_R c_{p,R} A_{q,R}} \cdot \left(T_w(t,z) - T_R(t,z)\right) \; ; \; z \in (0, L) \tag{3a}$$

$$T_R(\cdot, 0) = T_{R,in} \tag{3b}$$

$$T_R(0, \cdot) = T_{R,0} \tag{3c}$$

The energy balance of the reactor wall $T_w(t,z)$ is described by (4), in which the conductive heat transport, the transfer term to the reaction medium, and the heat transfer to the heating jackets are considered. At the beginning and at the end of the reactor, the zero gradient boundary conditions (4b), (4c) are assumed.

$$\begin{aligned}\rho_w c_{p,w} \partial_t T_w(t,z) = {} & \lambda_w \partial_z^2 T_w(t,z) \\ & - \frac{kA_{R,w}}{A_{q,w}} \cdot \left(T_w(t,z) - T_R(t,z)\right) \\ & + \frac{kA_{w,J}}{A_{q,w}} \cdot \left(T_J(t,z) - T_w(t,z)\right)\end{aligned} \tag{4a}$$

$$0 = \partial_z T_w\big|_{z=0} \tag{4b}$$

$$0 = \partial_z T_w\big|_{z=L} \tag{4c}$$

$$T_w(0, \cdot) = T_{w,0} \tag{4d}$$

$$T_J(t,z) = \begin{cases} z_{heater,1,begin} < z \le z_{heater,1,end} : T_{J,1}(t,z) \\ z_{heater,2,begin} < z \le z_{heater,2,end} : T_{J,2}(t,z) \\ z_{heater,3,begin} < z < z_{heater,3,end} : T_{J,3}(t,z) \end{cases} \tag{4e}$$

The temperatures of the heating jackets $T_{J,i}(t,z)$ are described by the energy balances shown in (5). In the heating jacket, the flow is convection dominated. Heat transfer to the reactor wall and heat loss to the environment are considered. The heating jacket is separated into three different sections i heated by the three different heaters h_i, as shown in the reactor set-up. The PDEs are defined on the domain $z \in (z_{h,beg,i}, z_{h,end,i})$ from the beginning to the end of the heater h_i for all three heaters. $T_{h,i}$ is the temperature of the heating baths.

$$\begin{aligned}\partial_t T_{J,i}(t,z) = {} & -v_{J,i} \partial_z T_{J,i}(t,z) \\ & - \frac{kA_{E,J}}{\rho_J c_{p,J} A_{q,J}} \cdot \left(T_{J,i}(t,z) - T_w(t,z)\right) \\ & - \frac{kA_{w,J}}{\rho_J c_{p,J} A_{q,J}} \cdot \left(T_{J,i}(t,z) - T_E(t,z)\right) \\ & z \in (z_{heater,i,begin}, z_{heater,i,end})\end{aligned} \tag{5a}$$

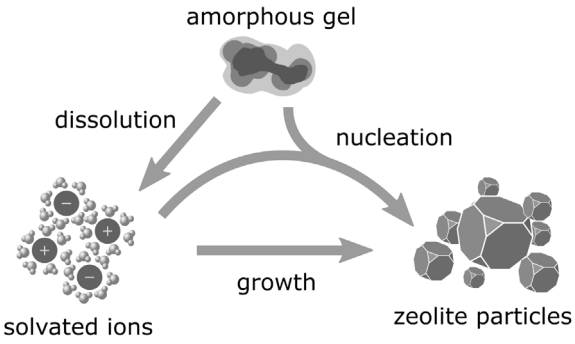

Fig. 2. Schematic of the zeolite crystallization steps.

$$T_{J,i}(\cdot, z_{heater,i,begin}) = T_{h,i} \; \forall i \in [1,3] \tag{5b}$$

$$T_J(0, \cdot) = T_{J,0} \tag{5c}$$

3.3. Zeolite crystallization

The zeolite crystallization model is a modified version of the model from Nikolakis et al. [22] based on the basic work of Thompson and Dyer [33] and Bhatia and Perlmutter [34].

The model describes the concentration of zeolite unit cells. The alumina and silicate feed streams form a solid gel phase that consists of amorphous particles which are formed instantaneously after the mixing step. In the crystallization reaction, the structural change of the amorphous to a crystalline solid phase takes place. The main reaction steps in this transition are shown in Fig. 2. First, the amorphous phase dissolves in the liquid phase. Then the supersaturation leads to a heterogeneous nucleation on the surface of the amorphous gel particles. The formed nuclei grow dependent on the supersaturation, to form the crystalline zeolite particles.

A basic assumption of the model is that the molar densities of the solid and the liquid phase, as well as the overall molar density, are constant. This holds true since the concentration of the dissolved unit cells is small.

3.3.1. Dissolution

First, the dissolution step is modeled. The dissolution of the amorphous solid is a comparably fast step [35]. The dissolution rate of

the amorphous solid, $H(t,z)$ is assumed to depend linearly on the concentration difference between the liquid concentration $C_{sol}(t,z)$ and the equilibrium concentration of the amorphous solid in the liquid $C_{eq,am}$. This was validated in lab measurements by Antonic and Ci [36]. In lab studies, the reaction order of the amorphous solid concentration C_{am} for the dissolution step was found to be 0.67 [36]. However, here a linear dependency of the amorphous solid concentration $C_{am}(t,z)$ on the rate of dissolution was used, similar to [33] since there is almost no effect of the dissolution order on the overall progress of the crystallization. The mathematical expression of the dissolution rate is given by (6):

$$H(t,z) = k_H(t,z) \cdot (C_{sol}(t,z) - C_{eq,am}) \cdot C_{am}(t,z). \tag{6}$$

The component balances of the zeolite unit cells of the amorphous solid $C_{eq,am}$ and of the dissolved ions $C_{sol}(t,z)$ are described by the transport Eq. (1) with the reaction rates shown in Eqs. (7)–(8). $\dot{C}_{zeo}$ is the molar crystallization rate.

$$\kappa_{am}(t,z) = -H(t,z) \tag{7}$$

$$\kappa_{sol}(t,z) = H(t,z) - \dot{C}_{zeo}(t,z) \tag{8}$$

The number density function of the zeolite particles $n(t,z,l)$ of particle size l is modeled analogous to [21,22]. It can be described by the transport Eq. (1) for $n(t,z,l)$ combined with the population balance Eq. (9). Heterogeneous nucleation with the rate $B(t,z)$ and growth with the growth rate $G(t,z)$ are assumed.

$$\kappa_n(t,z,l) = -\partial_l\left[G(t,z)n(t,z,l)\right] + B(t,z) \cdot \delta(l) \tag{9}$$

3.3.2. Nucleation

In the zeolite community, there is a debate about the nature of nucleation in zeolite crystallization. Homogeneous [21], heterogeneous [37], or autocatalytic [37–39] processes are assumed. Furthermore, alternatives approaches assume the formation of a secondary amorphous phase that induces nucleation [1]. In this work, the nucleation is assumed to take part at the inner surface of the amorphous solid, analogous to the approach developed by Nikolakis et al. [22]. However, this requires precise knowledge about the pore distribution in the amorphous gel network, which is not measurable in reality. Furthermore, the structure of the model equations which involves the calculation of a squareroot over a logarithmic ratio can lead to infeasible solutions in case of numerical errors, which makes it difficult to include in distributed parameter systems and hard to use in optimization algorithms. Therefore, the model was modified. A description of this novel nucleation model is given in the following. A detailed derivation is provided in Appendix A.1.

The heterogeneous nucleation rate is described by (10), as a function of an active inner surface of the amorphous solid S. The effect of the mass transfer to the active inner surface is neglected since the simultaneous dissolution on the surface leads to short diffusion lengths. Therefore, the nucleation step determines the overall nucleation rate. The nucleation rate B is assumed to depend also linearly on the supersaturation, which is the difference between the equilibrium concentration and the concentration of the zeolite in the liquid $C_{eq,zeo}$. The particle size of the nuclei is assumed to be zero.

$$B(t,z) = k_B(t,z) \cdot S(t,z) \cdot (C_{sol}(t,z) - C_{eq,zeo}) \tag{10}$$

For the description of the evolution of the inner surface of the amorphous solid S a description of the evolution of the inner pores is used similar to [34]. It is assumed that the active surface is a result of non-overlapping cylindrical pores with the size distribution $\varsigma(r)$ dependent on the pore radius r. The evolution of the pore size distribution $\varsigma(r)$ can be described using the population balance (11).

$$\partial_t \varsigma(t,r) + \partial_r\left[\varsigma(t,r)\frac{dr}{dt}\right] = \Gamma(t,\varsigma) \tag{11}$$

Under the assumption that the amount that is dissolved in the considered pores is much smaller than the overall dissolved amorphous solid, the general loss term $\Gamma(t,\varsigma)$ is defined by the dissolution reaction, and the population balance Eq. (11) can be solved using the method of moments. A detailed description of the nucleation model is given in Appendix A.1. The evolution of the inner volumetric surface area of the amorphous solid pore network along the reactor S can be described by the reaction rate (12).

$$\kappa_S(t,z) = k_H \cdot (C_{eq,am} - C_{sol}(t,z)) \cdot (K_C C_{am}(t,z) - S(t,z)) \tag{12}$$

During the dissolution of the amorphous solid, the radii of the pores in the amorphous gel network grow, which leads to larger surface areas. On the other hand, with decreasing amount of solid, the surface area decreases. The nucleation rate curve depends on the positive constant K_C. For low values of K_C, the behavior is similar to heterogeneous nucleation. For a high value of K_C the nucleation behavior is similar to an autocatalytic nucleation mechanism. A graphical visualization is shown in Appendix A.2.

The predicted nucleation behavior matches that of the model by Nikolakis et al. [22]. The rapid increase of the crystallinity after a certain induction time in which almost no formation of crystals takes place can be captured.

3.3.3. Growth

The growth rate G of the zeolite particles is modeled as a linear function of the supersaturation and independent of the particle size l. These assumptions have been validated by Subotić and Antonić [40] and Lechert and Kacirek [41].

$$G(t,z) = k_G(t,z) \cdot (C_{sol}(t,z) - C_{eq,zeo}) \tag{13}$$

The kinetics of the zeolite crystallization is dependent on the temperature of the solution T_R. This influence is described by an Arrhenius dependency:

$$k_i = k_{i,0} \exp\left(\frac{-E_{A,i}}{RT_R}\right) \quad i = H, B, G, \tag{14}$$

Since the growth rate is independent of the particle size l, the population balance Eq. (9) can be transformed using the method of moments where the moments are given by (15).

$$\mu_i = \int_0^\infty l^i n dl \tag{15}$$

The resulting reaction rates for the different moments μ_i are shown in Eq. (16):

$$\kappa_{\mu_0}(t,z) = B(t,z) \tag{16a}$$

$$\kappa_{\mu_1}(t,z) = G(t,z) \cdot \mu_0 \tag{16b}$$

$$\kappa_{\mu_2}(t,z) = 2 \cdot G(t,z) \cdot \mu_1 \tag{16c}$$

$$\kappa_{\mu_3}(t,z) = 3 \cdot G(t,z) \cdot \mu_2. \tag{16d}$$

The molar crystallization rate $\dot{C}_{zeo}$ then results as

$$\dot{C}_{zeo}(t,z) = \frac{\pi}{6v_m}\kappa_{\mu_3}(t,z). \tag{17}$$

The crystallinity of the solid X is defined in (18) as the ratio of the mass of the crystalline phase over the total mass of solids. The small number ϵ is added to avoid numerical issues when simulating the startup of the reactor, since then $C_{zeo}(t,z)$ and $C_{am}(t,z)$ are small.

$$X(t,z) = \frac{C_{zeo}(t,z)}{C_{zeo}(t,z) + C_{am}(t,z) + \epsilon} \tag{18}$$

The ratios of the moments represent the relevant mean the particle sizes

$$\bar{l}_{i,j} = \frac{\mu_i}{\mu_j}. \tag{19}$$

To improve the numerical properties of the model, the concentrations are scaled. The concentration of the amorphous solid and the concentration of the dissolved solid mass are scaled with the overall solid concentration. The particle size is scaled such that the calculated characteristics defined by Eq. (19) at complete conversion are close to one. Furthermore, the moment equations are scaled such that the third moment is equal to the scaled zeolite concentration. The inner surface of the particles is scaled such that the initial inner zeolite surface area is equal to one. The scaling is discussed in more detail in Appendix B.2.

3.4. Summary

The complete model of the reactor consists of the convection–diffusion balance Eq. (1) for the mass balances with the reaction terms for the different components according to (8), (7), (12), (16a)–(16d) coupled with the energy balances (3), (4), (5). The implemented scaled model equations are summarized in Appendix B.

The resulting system of 10 partial differential equation is solved using the method of lines. The spatial domain is discretized using the weighted essentially nonoscillatory (WENO) discretization scheme [42,43] on 104 grid points. This approximation is used due to its lower tendency to produce oscillating solutions for convection dominated systems. After discretization, the resulting model is a system of nonlinear ordinary differential equations for the conserved quantities T_R, T_w, T_J, $C_{am}, C_{sol}, S, \mu_0, \mu_1, \mu_2, \mu_3$ along the reactor length, which results in 1040 state variables. In the following, the model will be referred to by (20), with x as states and u as the inputs, which are the set-point temperatures of the three heaters T_h and the throughput F of the reactor.

$$\dot{x} = f(x, u) \tag{20}$$

The model has been implemented in the CasADi [44] framework in a python programming environment.

4. Model validation

4.1. Methodology

The different elements of the model, mass transfer, energy transfer, and the zeolite formation kinetics, are verified separately. First, several unknown parameters of the model are fitted to experimental data. Then the fit is validated using a statistical analysis. For the parameter fit, the least squares optimization problem (21) is solved.

$$\min_{p,x} \sum_{k}^{N_{exp}} \sum_{j}^{N_{meas,k}} \sum_{i}^{N_{time,k,j}} \frac{1}{N_{exp} N_{meas,k} N_{time,k,j}} \left(\frac{y_{k,j} - \hat{y}_{k,j,i}}{\sigma_{k,j,i}} \right)^2 \tag{21a}$$

s.t.

$$\dot{x}_k(t) = f_k(x_k(t), u_k(t), p) \qquad \forall k \in [0, N_{exp}] \tag{21b}$$

$$y_{k,j,i} = h_{k,j}(x_k(t_i), u_k(t_i), p) \quad \forall k \in [0, N_{exp}],$$
$$\forall j \in [0, N_{meas,k}], \forall i \in [0, N_{time,k,j}]. \tag{21c}$$

In (21) the model parameters p are optimized such that the mean squared error between the model predictions $y_{k,j,i}$ and the measurements $\hat{y}_{k,j,i}$, scaled with the variances of the measurement errors $\sigma_{k,j,i}$ is minimized. The predicted measurements are calculated from the model states by using the functions $h_{k,j}$. There is a total number N_{exp} of experiments with $N_{meas,k}$ different measurements j for all $N_{time,k,j}$ time points i.

The optimization problem is implemented in a python environment. A single-shooting approach is used as a solution approach for the dynamic optimization problem. The ordinary differential model equations are solved with the IDAS [45] solver with the CasADI [44] interface. The (low dimensional) optimization problem is solved using the derivative-free local optimizer [46] which uses a Nelder–Mead-type algorithm. The reason for the usage of this solver with a comparably slow convergence rate is the robustness against local minima which are present due to the dense structure of the optimization problem and due to the measurement errors. Higher order solvers, e.g., Levenberg–Marquardt, were found to be more prone to find suboptimal solutions, which can be explained by the approximation errors of the involved calculations of derivatives by finite differences. To minimize the effect of local minima, the solver is started from different initial points.

The results are then validated using statistical methods. The match between the observations and the estimates is tested using the reduced chi-squared value. The goodness of fit is validated with Pearson's chi-squared test [47]. The covariance matrix Σ of the fitted parameters is estimated by (22).

$$\Sigma^{-1} = J(p^*)^T J(p^*) \tag{22}$$

J is the Jacobian of the vector of residuals, scaled with the standard deviations, with respect to the measurements evaluated at the optimal solution p^*. The confidence intervals for the fitted parameters are calculated using the equation below.

$$\Delta p_i = t_{\alpha,\nu} \sqrt{\Sigma_{i,i}} \tag{23}$$

Where $t_{\alpha,\nu}$ is the quantile of the t-distribution with the confidence level α and ν degree of freedom. For the statistical tests and the confidence intervals, the confidence level is 95%.

4.2. Mass transport

For the zeolite reaction, the most important mass transport related quantity is the transport of the zeolite particles since the concentration of dissolved solid in the mother liquor is comparably low, and the dissolution is fast. Therefore, the residence time distribution of the solid was measured during the startup of the reactor for several experiments with different throughputs. The frequency of oscillation (1.5 Hz) and amplitude (34 mm) of oscillation were kept constant. The correlations for the back mixing from the literature [48,49] propose a almost linear dependency of the Reynolds number on the Schmidt number, which leads to a constant Peclet number with changing throughput. Therefore, we use a constant Peclet number independent of the flow rate. For a variation of the frequency or the amplitude of the oscillation of the COBR, which is not considered in this work, the Peclet number has to be adapted accordingly to the reported dependencies. The measured concentration of solid over time is normalized with the expected solid concentration and with the residence time. The solution of the least squares minimization problem with the estimated confidence bound is

$$Pe = 240.2 \pm 32.02. \tag{24}$$

The fit was performed from 10 different initial points, sampled from a Latin hypercube within a reasonable parameter range. All optimization runs lead to the same solution. The reduced chi-square value is 0.826, which is close to one, which indicates that the expected noise matches the observed error. This was validated in Pearson's chi-squared test, in which the null hypothesis was accepted that the distributions are the same. The fitted and the measured relative concentrations as a result of a step input change of solid concentration for the different experiments are displayed in Fig. 3, which displays a good fit of the experimental findings and the model.

4.3. Energy balance

In order to parameterize the description of the thermal behavior, the model was fitted to measured data from five different dynamic experiments. In these experiments, the heater temperatures were changed and the response of the temperature along the reactor was measured. The temperature is measured by 11 different temperature measurements

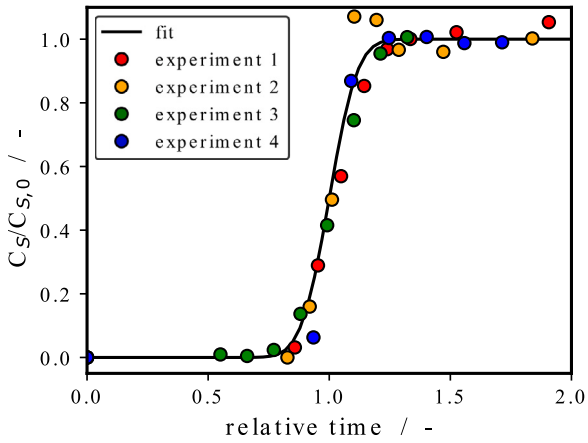

Fig. 3. Fitted and experimentally measured concentration of solid particles as a result of step input change of solid concentration for different flowrates.

Table 1
Correlation coefficients from the fit of the thermal parameters.

Correlation coefficients	
	$kA_{R,w,b}$
$kA_{R,w,f}$	−0.00189

which are equally distributed along the reactor length in the reaction solution. In the parameter fit, only the heat transfer coefficient from the reaction solution to the wall $kA_{R,w}$ is adjusted. It was observed that $kA_{R,w}$ changes over the reactor length. This is most probably due to the changing properties of the suspension in the reactor. The viscosity of the suspension changes according to a complicated pattern within the reactor. First, it increases from a medium viscosity to a high viscosity at the beginning of the reactor and then drops to a lower viscosity at the end of the reactor. In order to decrease the complexity, we assume that, the heat transfer coefficient changes at the beginning of the last heating section, in which the reaction medium is cooled. Upstream of this point, the value $kA_{R,w,b}$ is used, downstream of this point the value $kA_{R,w,f}$. The heat transfer coefficients from jacket to wall $kA_{j,w}$ and the loss to the environment are approximated by standard correlations. The sensitivity of the measured temperatures to these parameters is low. Therefore, they are not included in the parameter fit. The solution of the least squares minimization problem, including the estimated confidence bound, is given in (25). The fit was performed from 10 different initial points within a plausible parameter range, sampled from a Latin hypercube. All runs led to the same solution.

$$kA_{R,w,b} = 228.673 \pm 0.409 \text{ W/m}^2\text{K} \tag{25a}$$

$$kA_{R,w,f} = 983.122 \pm 5.694 \text{ W/m}^2\text{K} \tag{25b}$$

The reduced chi-square value is 0.891, which is close to one, which indicates that the expected noise matches the observed error. This was validated using Pearson's chi-squared test, in which the null hypothesis was accepted that the distributions are the same. The correlation coefficient between the two fitted parameters fit is shown in Table 1. The correlation coefficient is very close to zero, which indicates that the uncertainties of both parameters are not correlated.

The fitted and the measured temperatures for one of the experiments are displayed in Fig. 4, which shows a good fit of the experimental findings and the model. The corresponding input trajectories are shown in the orange plots. The deviations at the start of the experiment occurred due to the mismatch in the initialization of the temperatures along the reactor. Deviations close to the inlet of the reactor are caused by a variation in the reactor inlet temperature. The dynamic responses to the changes of the heater temperatures are described accurately.

4.4. Zeolite crystallization

Finally, the model of the zeolite crystallization was validated. First, model predictions were fitted to seven different experiments. In these experiments, different operating points, defined by heater temperatures and the throughput, including dynamic step changes, were considered. The zeolite properties were measured in an offline fashion by taking samples at different positions of the reactor. The crystallinity was measured by X-ray diffraction. The primary particle size of the zeolites was measured by laser diffraction. For more details about the zeolite characterization, the reader is referred to Ramire. Mendoza et al. [17].

In the parameter fit, only a limited number of selected kinetic parameters of the zeolite crystallization process were fitted. The dissolution reaction is comparably fast. The concentration of unit cells in the solution is therefore constant in the nucleation phase and in most of the growth phase. Therefore, the influence of the dissolution rate constant k_H and of the activation energy $E_{A,H}$ cannot be observed, until the reaction becomes rate-determining, which does not happen in the considered temperature range. Therefore, this value is taken from the literature [36].

It was observed that the primary particle size of the zeolite particles was constant within the observed temperature range. This implies a constant ratio of nucleation and growth. Furthermore, the amount of data does not allow for the estimation of individual activation energies of nucleation and growth. Therefore, we assumed the same activation energy for nucleation and growth. The nucleation and growth rates k_B, k_g, the activation energy of nucleation and growth $E_{A,g}$, and the kinetic factor for the gel transition K_c were fitted to the experimental data. To simplify the fitting problem, the rates k_B, k_g are fitted at a predefined temperature $T_f = 373$ K. The solution of the least squares minimization problem, including the estimated confidence bounds, is given in (26). The fit was performed from 23 different initial points within a reasonable parameter range distributed on a Latin hypercube. The optimal solution was found in 9 of these runs. Therefore, this problem is more prone to local optima in contrast to the previously discussed problems. Since the optimal solution was found multiple times from different initial points, the result is considered as reliable.

$$k_B(T_f) = 0.0360649 \pm 0.001171 \text{ s}^{-1} \tag{26a}$$

$$k_g(T_f) = 0.0268283 \pm 0.0003366 \text{ s}^{-1} \tag{26b}$$

$$K_c = 0.00349242 \pm 0.03198 \tag{26c}$$

$$E_{A,g} = 78323.6 \pm 726.0 \text{ J/mol} \tag{26d}$$

The large confidence interval of the kinetic constant K_c is due to its relatively small value. Therefore, the influence of the increasing surface is rather small in comparison to the overall decrease due to the consumption of the amorphous solid. The observed activation energy matches data from literature, which gave activation energies of 66 kJ/mol and 72 kJ/mol [50]. The reduced chi-square value is 1.11, which is close to one, which indicates that the expected noise matches the observed error. This was validated by Pearson's chi-squared test, in which the null hypothesis was accepted that the distributions are the same. The correlation coefficient between the two fitted parameters fit is shown in Table 2. Since the values are tightly coupled, the corresponding correlation coefficient are high, especially of the nucleation and growth rate, but also of the growth rate and the activation energy.

The fitted and the measured concentrations for one of the experiments are displayed in Fig. 5. The corresponding input trajectories are shown in the orange plots. The figure displays a good fit of the experimental findings and the model. The deviations at the start-up of the reactor are due to the inevitable uncertainties in this phase. For example, the small deviations in the timing of the sampling are quite visible. Furthermore, the modeling assumptions e.g., constant solid content, are not valid during the reactor startup. The dynamics after the startup are predicted accurately.

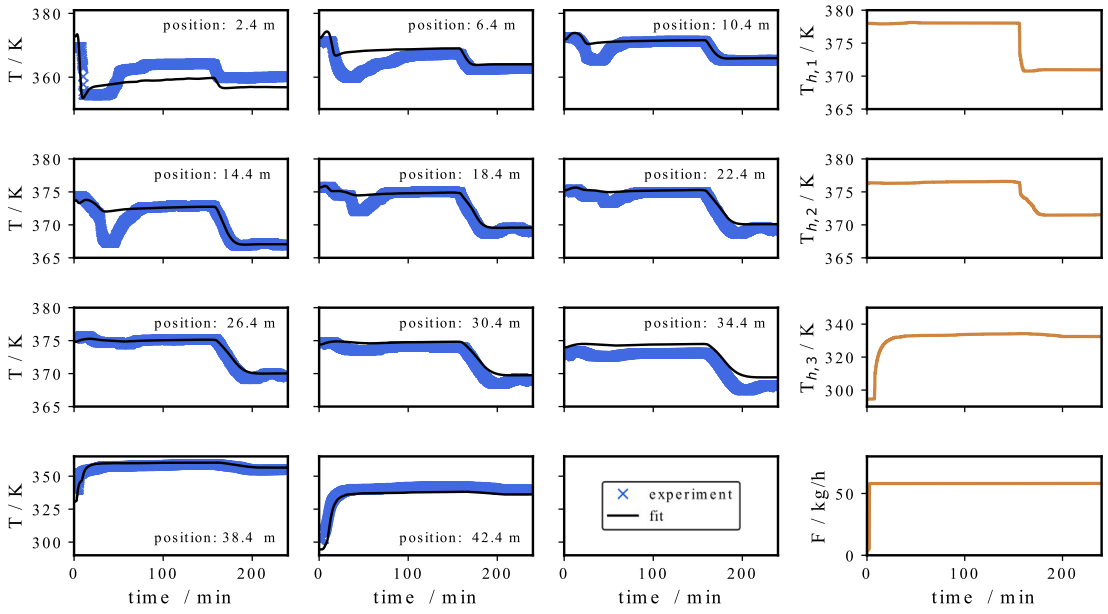

Fig. 4. Fitted and experimentally measured evolution of the temperatures along the reactor as a response to a step change of the heater temperatures.

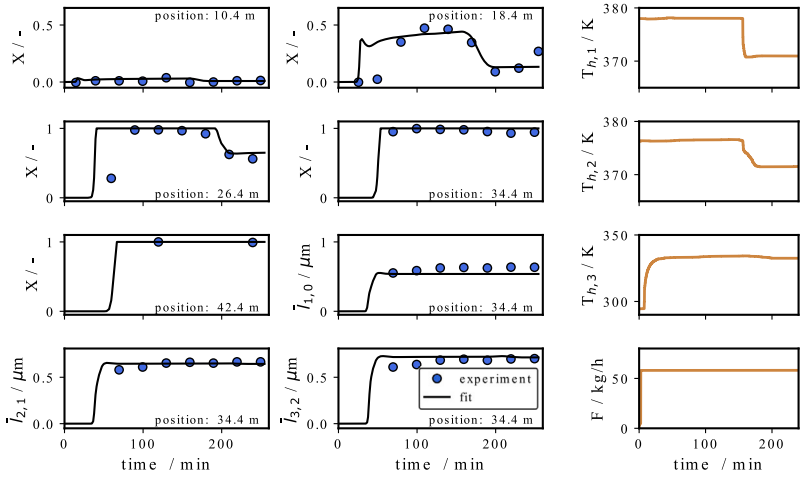

Fig. 5. Fitted and experimentally measured evolution of the crystallinity (X) along the reactor and of the mean particle size of the primary particles from the crystalline zeolite.

Table 2
Correlation coefficients from the fit of the kinetic parameters.

Correlation coefficients			
	k_B	k_g	K_c
k_g	−0.693149	–	–
K_c	−0.100258	0.0602252	–
$E_{A,g}$	0.0466702	0.413624	−0.256534

The validity of the developed model is demonstrated for the pilot-scale plant. For the description of an industrial-scale reactor, the model parameters have to be adapted and possibly further effect may have to be included.

5. Quantification of the model uncertainty

5.1. Methodology

In the previous chapter, it was shown that the system can be described accurately by the process model. However, due to structural mismatches and disturbances, the model predictions deviate from the real behavior. To quantify the deviations between the model and the real behavior, the covariance matrix of the parametric uncertainty at a steady state is determined. The steady state is considered here instead of the dynamic description since we can use the automatic differentiation of CasADi to get accurate estimates of the Jacobian and to avoid mismatches due to sample time errors. The parametric covariance matrix with respect to the uncertain parameters is computed using Eq. (27).

$$\Sigma_E^{-1} = \left(\frac{\partial y}{\partial x_{ss}}\frac{\partial x_{ss}}{\partial p}\right)^T \cdot \Sigma_y^{-1} \cdot \left(\frac{\partial y}{\partial x_{ss}}\frac{\partial x_{ss}}{\partial p}\right) \tag{27}$$

in which $\partial x_{ss}/\partial p$ is the sensitivity matrix of the steady state with respect to the parameters. This is projected via the Jacobian of the measurement functions from the steady states $\partial y/\partial x_s s$ to the measurements. The covariance of the measurements Σ_y is estimated from the experimental data of the steady-states. The parameters used to describe the plant-model mismatch are different from the previously identified parameters since the effect of external conditions, and disturbances should also be captured. Furthermore, we want to reduce the number of parameters

needed to describe the uncertainty. The uncertain parameters were chosen as a combined nucleation and crystallization rate (η) and offsets of the heater temperatures ($\Delta T_{h,i}$), and a deviation of the inlet temperature from the assumed value ($\Delta T_{R,in}$). The following equations of the model are modified

$$\tilde{G}(t,z) = G(t,z) \cdot 10^{\eta} \tag{28a}$$

$$\tilde{B}(t,z) = B(t,z) \cdot 10^{\eta} \tag{28b}$$

$$\tilde{T}_{R,in} = T_{R,in} + \Delta T_{R,in} \tag{28c}$$

$$\tilde{T}_{h,i} = T_{h,i} + \Delta T_{h,i} \quad \forall i \in [1,3]. \tag{28d}$$

The parameter vector p contains the uncertain parameters $p = (\eta, \Delta T_{R,in}, \Delta T_{h,1}, \Delta T_{h,2}, \Delta T_{h,3})$. To capture the effect of the parametric uncertainty on the system response, the unscented transform is used. Furthermore, the unscented transform is used to calculate the expected deviation and the expected variation of the system response from the nominal trajectory using the sigma points of the error parameter covariance matrix.

5.2. The unscented transform

The unscented transform [25] can be used to approximate the propagation of a Gaussian probability distribution p of dimension N through a nonlinear function, using the $2N + 1$ sigma points p_i.

$$p \sim \mathcal{N}(\bar{p}, \Sigma) \tag{29}$$

The sigma points can be calculated using Eq. (30). The square root is the lower Cholesky decomposition of the covariance matrix Σ. The index k represents the kth column. The parameter ϵ is a tuning parameter and determines the spread of the sigma points.

$$p_0 = \bar{p} \tag{30a}$$

$$p_k = \bar{p} \pm \sqrt{(N+\epsilon)\Sigma_k} \quad \forall k \in [0, 2N] \tag{30b}$$

The expected value and the covariance of the resulting probability distribution after the nonlinear transformation g can be estimated using the Eqs. (31), and (32)

$$\mathbb{E}[g(p)] \approx \sum_{k=0}^{2N} w_{m,k} g(p_k) \tag{31}$$

$$cov\Big[\mathbb{E}[g(p)] - g(p)\Big] \approx \sum_{k=0}^{2N} w_{c,k} (g(p_k) - \overline{g(p)})(g(p_k) - \overline{g(p)})^T. \tag{32}$$

The weights $w_{m,k}$ and $w_{c,k}$ are calculated using the Eqs. (33)–(34) analogously to [25].

$$w_{m,0} = \frac{\alpha^2 \cdot (N+\kappa) - N}{\alpha^2 \cdot (N+\kappa)} \tag{33a}$$

$$w_{m,k} = \frac{1}{2\alpha^2 \cdot (N+\kappa)} \quad \forall k \in [1, 2N] \tag{33b}$$

$$w_{c,0} = \frac{\alpha^2 \cdot (N+\kappa) - N}{\alpha^2 \cdot (N+\kappa)} + (1 - \alpha^2 + \beta) \tag{34a}$$

$$w_{c,k} = \frac{1}{2\alpha^2 \cdot (N+\kappa)} \quad \forall k \in [1, 2N] \tag{34b}$$

The distribution of the uncertain parameters is assumed to be close to a Gaussian distribution, therefore the parameters κ, β are set to the recommended values for such cases: $\kappa = 0$, $\beta = 2$. The spread of the sigma points α is chosen to be $\alpha = 1.54$, such that the sigma points are on the boundary of an ellipsoid that contains $\approx 96.3\%$ of the parameter realizations if they follow a normal distribution.

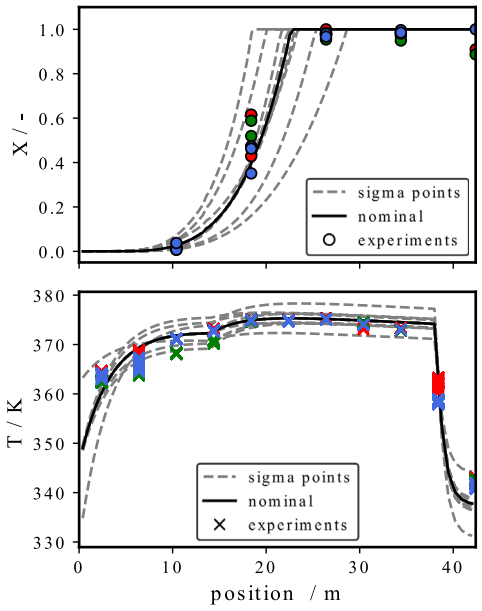

Fig. 6. Nominal profiles and profiles at the sigma point for a steady-state operation and in comparison to experimental data.

5.3. Quantification of the plant-model mismatch at steady state

The values of the covariance matrix from the uncertain parameters, the combined nucleation and crystallization rate, the offsets of the heater temperatures, and the deviation of the inlet temperature, are calculated as described in Section 5.1. The sigma points are calculated from this covariance matrix. The simulated nominal steady-state profile of the plant and the simulation results with the parameter values being at the sigma points are shown in Fig. 6 in comparison to multiple experiments of the same steady-state. The particle size is omitted here since it is not sensitive as product quality indications. The different experiments are displayed in different colors. The comparison shows that the model prediction and the experimental data match well in the steady state. Furthermore, it is visible that the chosen operation point is suboptimal. The operation point is too conservative since the crystallization is already completed in the middle of the reactor. The rest of the reactor is not used for the crystallization reaction. From the plot, it can also be seen that the additional space is not needed since the minimum of the predicted product quality according to the sigma points is reaching the required product quality at around 28 m, which is also supported by the crystallinity measurements at that point. Therefore, the shown operation point can be improved, the throughput can be increased or the applied energy input can be decreased, or the process can be performed in a smaller reactor set-up.

5.4. Validation of the quantification of the plant-model mismatch in dynamic simulations

The error quantification led to a set of scenarios for the behavior at the steady state. As the next step, the error in the prediction of the dynamic behavior is analyzed. The nominal system trajectory and the spread of the predictions for the parameters taking values at the sigma points are displayed in Fig. 7 in comparison to experimental data. The respective input trajectories are shown in the orange plots. The error of the model is captured well by the sigma points. The uncertainty of the crystallinity trajectory lies within the envelope of the trajectories that are obtained for the parameters taking values at the sigma points. The spread of the predictions for the different sigma points is large in the region of intermediate crystallinity. At low crystallinity and at

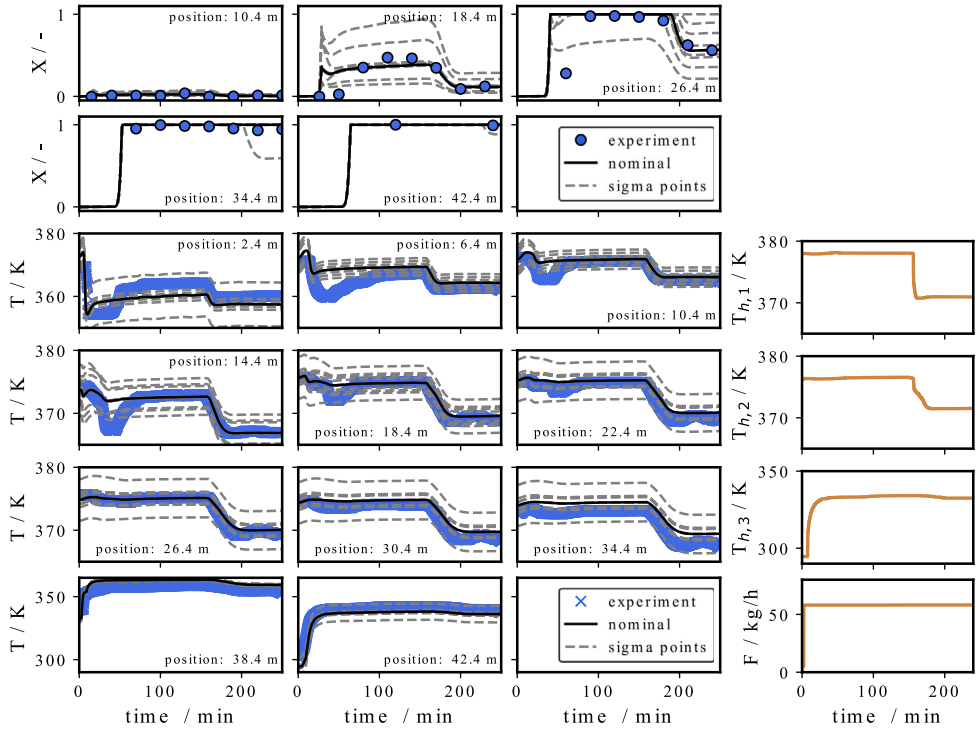

Fig. 7. Nominal and sigma point based predicted trajectories of the conversion and the reactor temperature of the COBR and experimental data.

full conversion, the spread decreases. Furthermore, the spread that is predicted using the sigma points is different for the positive and the negative direction. This is a major advantage of performing the error propagation using the unscented transform by which this behavior can be predicted correctly. The thermal behavior is also be captured correctly for the most part. However, there is a visible deviation during the startup of the rector so the model cannot be considered to be reliable at the startup. This however does not affect the computation of the optimal operation. There is no visible nonlinearity in the error propagation for the thermal behavior and the temperature deviation can be described well. The description of the plant-model mismatch is thus also valid for dynamic set-point changes, except for the initial phase at reactor startup.

6. Robust optimization of the operation of the COBR

6.1. Problem statement

In the following, the steady-state performance of the zeolite crystallization process in the COBR is optimized such that at a given throughput, the product quality constraints are fulfilled for all scenarios (sigma points) with minimum expected energy input. The energy consumption of the process is defined by the temperature difference between heating and cooling fluid at the inlet and the outlet of the heaters. It is assumed that for heating and cooling, the same external input of energy is required, therefore absolute values are used in (35). Additionally, the energy input via the material flow is considered as shown in Eq. (35), in which $T_R(\cdot,0)$ is the inlet temperature of the reactor and T_E is the environment temperature.

$$E(x,u,p) = \sum_{i=1}^{3} \dot{m}_J c_{p,J} |T_J(\cdot, z_{h,out,i}) - T_{h,i}| + \dot{m}_R c_{p,R} \cdot |T_R(\cdot,0) - T_E| \tag{35}$$

The formulation of the optimization problem is stated in (36). The approximation of the expected energy input by the unscented transform is minimized by summation over the sigma points, see (36a).

$$\min_{u,X} \left[\mathbb{E}(E(x,u,p)) \approx \sum_{k=0}^{2N} w_{m,k} E(x_k,u,p_k) \right] \tag{36a}$$

s.t.

$$0 = f(x_k,u,p_k) \quad \forall k \in [0,2N] \tag{36b}$$

$$382.15 \geq T_{R,k}(\cdot) \quad \forall k \in [0,2N] \tag{36c}$$

$$353.15 \geq T_{R,k}(L) \quad \forall k \in [0,2N] \tag{36d}$$

$$0.98 \leq X_k(L) \quad \forall k \in [0,2N] \tag{36e}$$

$$393.15 \geq T_{h,i} \quad \forall i \in [1,3] \tag{36f}$$

$$F_{fix} = F \quad \forall i \in [1,3] \tag{36g}$$

The process is constrained to be at the steady state for all sigma points by (36b). The temperature of the reaction solution should be lower than 382.15 K to suppress the formation of undesired zeolite phases. This is enforced for all sigma points by (36c). Furthermore, the outlet temperature has to be lower than 353.15 K for the downstream processing. Similarly, the desired crystallinity of 98% at the reactor outlet should be reached for all sigma points, see (36e). The heater temperatures of the three heaters are limited to 393.15 K to avoid bubble formation in the reactor with a fixed pressure (36f). The throughput of the reactor is fixed (36g), but the optimization is performed for multiple throughputs between 34.2 kg/h, which is the lower limit due to the sedimentation of the particles, and 91.2 kg/h, which is the maximal stable operating point of the feed pumps. Since the throughput of the reactor is fixed, the degrees of freedom are the heater temperatures.

6.2. Implementation

The optimization is solved in CasADI [44] in a python framework by the NLP solver Ipopt [51], including the linear solver HSL MA27 [52]. For a smooth approximation of the absolute value in the objective function, the tanh sigmoid function is used, as shown in Eq. (37):

$$|x| \approx \tanh(x \cdot \beta) \cdot x. \tag{37}$$

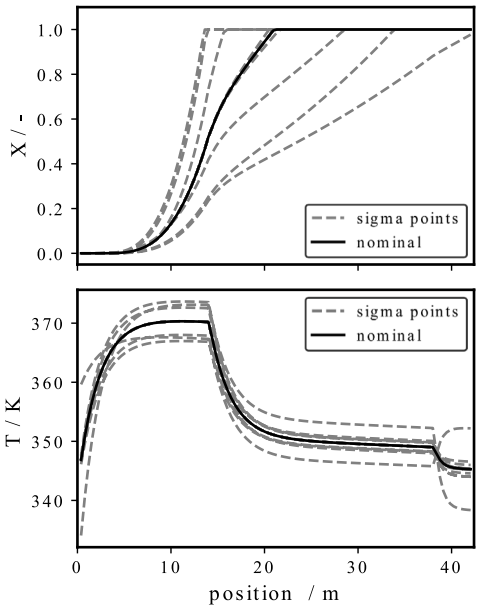

Fig. 8. Optimized steady state profiles for the nominal model and for the model predictions with the sigma points for a low throughput of 34.2 kg/h.

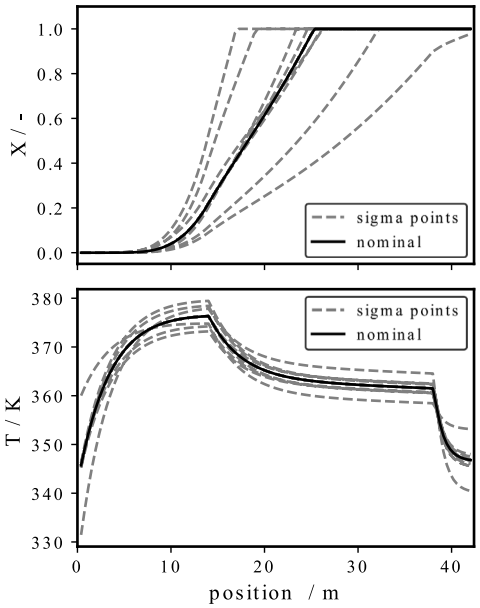

Fig. 9. Optimized steady state profiles for the nominal model and for the model predictions with the sigma points for a medium throughput of 57.0 kg/h.

The factor β determines the accuracy of the approximation. A value of 100 was found to be sufficient.

6.3. Optimization results

The resulting optimal profiles of the crystallinity and of the reactor temperature are shown in Fig. 8 for a low throughput (34.2 kg/h), in Fig. 9 for a medium throughput (57.0 kg/h), and in Fig. 10 for the highest possible throughput (91.2 kg/h).

The optimal operation of the reactor for all throughputs has the following structure: The medium is heated up at the beginning of the reactor. The maximal temperature is reached at the end of the first heating section at 18.4 m. The second heating jacket is operated at a lower temperature. The temperature therefore drops until an

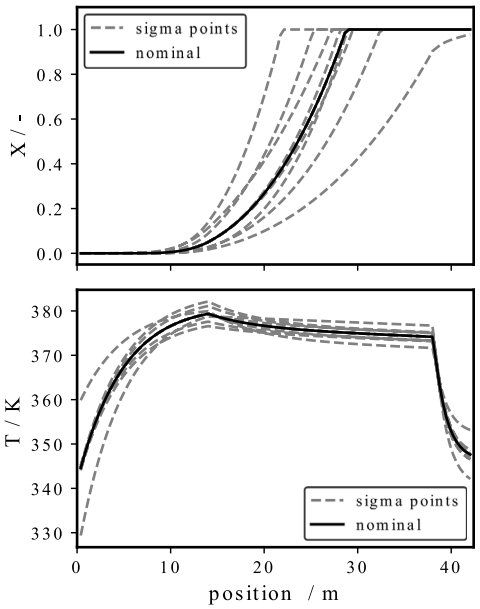

Fig. 10. Optimized steady state profiles for the nominal model and for the model predictions with the sigma points for the highest possible throughput of 91.2 kg/h.

equilibrium temperature is reached at approximately 25 m. With the third heater, the reaction medium is cooled down further to satisfy the specifications of the outlet temperature.

This structure is the same for all throughputs, however in the lowest throughput, the heating medium is only heated such that the highest temperature among the cases described by the sigma points has a maximum at around 375 K, therefore the maximum temperature constraint is not active in this case. In the medium and high throughput cases, the reactor content is heated to the maximum feasible temperature for the highest of the sigma point based predictions. Furthermore, with increasing throughput, the temperature of the second heater is increased, which leads to a smaller temperature variation at the beginning of the second heating area. For the high throughput case, the temperature profile is almost constant in this area.

The crystallinity profiles depend on the temperature profiles. For all optimal operating points, only the quality constraint for the case with the lowest crystallinity is active. For higher throughputs, the crystallization is shifted towards the end of the reactor. Furthermore, for higher throughput, the spread of the trajectories decreases, which indicates that the process is more robust at higher throughputs.

6.4. Evaluation of the probability of constraint violations

Strictly speaking, meeting the constraints for the sigma points does not ensure to meet a probabilistic specification or robust constraint satisfaction over the range of all parameter uncertainties. Therefore, in this section, we investigate the probability of constraint violations for the optimized operating points precisely. The steady state profiles are calculated for 100,000 parameter realizations drawn from a multivariate normal distribution with the given parameter covariance matrix. The evaluation leads to a feasibility of the low throughput operating point for 99.66% of the sampled parameter realizations, for the medium throughput operating point for 99.84%, and for the high throughput operating point for 99.70%. The reason that these values are higher than the probability that underlies the choice of the sigma points is because the inequality constraints only become active at specific combinations of parameters, e.g., a very high crystallization rate does not lead to a constraint violation. In conclusion, the application of the calculated optimal operating points to the process can be expected to lead to an admissible operation in all cases.

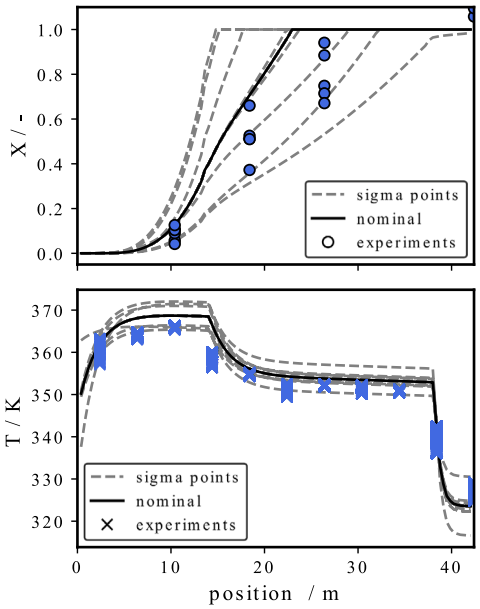

Fig. 11. Nominal and sigma point based predictions of steady state profiles and measurements of the steady state profile for the optimized operating conditions at a low throughput of 34.2 kg/h.

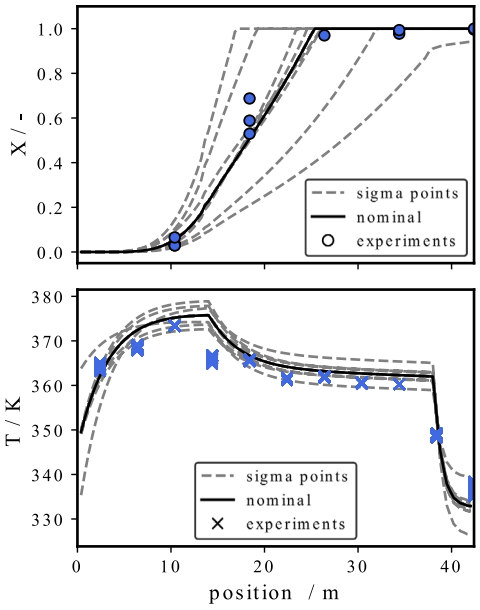

Fig. 12. Nominal and sigma point based predictions of steady state profiles and measurements of the steady state profile for the optimized operating conditions at a medium throughput of 57.0 kg/h.

6.5. Application to the real process

In the following, the results of applying the optimal operating points to the real pilot scale process are presented. The resulting profiles and the experimental results are shown in Fig. 11 for the low throughput (34.2 kg/h), in Fig. 12 for the medium throughput (57.0 kg/h), and in Fig. 13 for the high throughput (91.2 kg/h).

The suitability of the operating points is confirmed. The operating points do not violate the requirements on the crystallinity or on the maximal temperatures. Furthermore, the higher stability of the process at the operating point with the maximal throughput, which was already observed in the optimization results, is also visible in the experimental

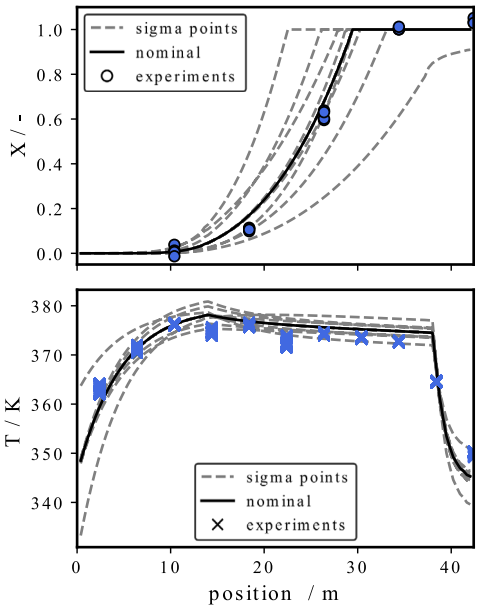

Fig. 13. Nominal and sigma point based predictions of steady state profiles and measurements of the steady state profile for the optimized operating conditions at a high throughput of 91.2 kg/h.

results since the spread of the measured crystallinity is lower in this case. At the pilot plant, the optimum operation could not be implemented exactly. Due to technical difficulties, the third heater inlet temperature had to be set to a lower value of 321.15 K, which leads to a higher drop in the temperature at the end of the reactor. This influences only the end of the crystallization process, but it is visible in the results since the simulated product quality does not reach the desired value for all sigma points. The real process however meets the specification.

The successful application proves the extrapolation capability of the rigorous model and the value of the robust optimization method. The model was developed and fitted mainly with data from the medium throughput operating point, and no feasible operating point at high or low throughputs had been identified previously. The energy demand, estimated from the sigma point based model predictions, of the optimized operating point at medium throughput is 6.76 kW. The estimated expected energy demand at the original operating point with the same throughput, as shown in Fig. 6, is 7.62 kW, which saves approximately 11.3% of the energy input.

This however is only a lower bound to the possible improvement as the optimal operation could not be implemented fully due to the problem with the third heater. Further potential lies in the application of feedback control techniques which can reduce the effect of model plant mismatches. This is promising especially for the thermal system, since the temperature measurements are already available. In the case of persistent model plant mismatch which is not caused by stochastic fluctuations, real time optimization with modifier adaptation techniques can be applied to improve the operation of the plant as demonstrated by Cegla et al. [53] for reactive extrusion.

7. Conclusion

This work presents the modeling, model validation, and robust optimization to calculate optimal steady-state operating points for an improved performance of the novel continuous zeolite production process in a continuous oscillatory baffled reactor (COBR). First, the process set-up, the quality and production constraints and the control variables with their individual bounds were introduced. Afterwards, the modeling of mass transport, energy transport and zeolite crystallization reaction in the COBR was presented. The mass transport in the COBR

is described by the axial dispersion model. The zeolite crystallization is described by a reaction term in the mass transport PDE. The zeolite crystallization model is a first principle model based on the solution the population balances with the method of moments. The nucleation model is a novel modified version of the heterogeneous nucleation model developed by Nikolakis et al. [22].

The model parameters were fitted to experimental data for the mass transport, the energy transport, and transfer, and the zeolite reaction individually. The validity of the fits were proven using Pearson's chi-squared test. Furthermore, the confidence intervals of the parameters were evaluated. The model gives an accurate description of the plant dynamics.

Afterwards, the plant-model mismatch was described by a parametric uncertainty of selected parameters. The unscented transform was used to propagate the parametric error and to get an estimate of the expected outcome and an estimate of the variation of the model predictions.

The model with the parameter values obtained from the sigma points of the unscented transform was then used in a robust optimization in which operating points with the minimal expected energy input are calculated that satisfy the constraints for all combinations of parameter values that were considered. This introduces a simple way to ensure the robustness of the operating point while avoiding unnecessary conservatism. The suitability of the approach was validated by the experimental application to the pilot-scale COBR process. Three optimal operating points at low, medium, and high throughputs were identified. These were applied to the pilot scale process. All operating points were proven to meet the specifications in the experiments.

Further work will use the dynamic model with the unscented-transform-based error model for a robust dynamic operation e.g., in transitions between operating points or in a demand side management setting. Additionally, optimization including feedback control based on online measurements will be used to reduce the fluctuations of the process.

Funding

The project leading to this publication has received funding from the European Union's Horizon 2020 research and innovation programme under grant agreement No. 820716. (project SIMPLIFY) and No. 101058279 (project SIMPLI-DEMO).

CRediT authorship contribution statement

Robin Semrau: Writing – original draft, Validation, Software, Methodology, Investigation, Conceptualization. **Heidy Ramirez Mendoza:** Writing – review & editing, Validation, Data curation. **Cécile Lutz:** Writing – review & editing, Project administration, Funding acquisition. **Sebastian Engell:** Writing – review & editing, Supervision, Funding acquisition, Conceptualization.

Declaration of competing interest

The authors declare the following financial interests/personal relationships which may be considered as potential competing interests: Dr. Lutz and Dr. Ramirez Mendoza are employed by the ARKEMA Company. Dr. Lutz is listed as inventor in ARKEMA patents in the field of the COBR. The other authors, they declare that they have no known competing financial interests or personal relationships that could have appeared to influence the work reported in this paper.

Data availability

The data that has been used is confidential.

Acknowledgments

Special gratitude is expressed to Mr. Yvan Lecomte and Ms. Sylvie Szendrovics for the supervision of the experiments and their technical advice.

Appendix A. Kinetic model

A.1. Evolution of the inner surface area

For the description of the evolution of the inner surface of the amorphous solid S, a description of the evolution of the inner pores is used similar to [34]. It is assumed that the active surface is a result of non-overlapping cylindrical pores with the size distribution $\varsigma(r)$. r is the radius of the pores and $\varsigma(r)$ is the combined length of all cylindrical pores with a given radius r per unit volume of the reaction mixture. The evolution of the pore size distribution $\varsigma(r)$ can be described using the population balance (11)

$$\partial_t \varsigma(t,r) + \partial_r\left[\varsigma(t,r)\frac{dr}{dt}\right] = \Gamma(t,\varsigma) \tag{A.1}$$

with the boundary conditions:

$$\varsigma(t,0) = 0 \tag{A.2}$$

$$\varsigma(t,\infty) = 0. \tag{A.3}$$

The local dissolution is assumed to be proportional to the local pore surface and is assumed to depend linearly on the concentration difference. The rate of pore growth over time is expressed by Eq. (A.4).

$$\frac{dr}{dt} = k_S(t)\cdot(C_{sol}(t) - C_{eq,am}) \tag{A.4}$$

The dissolution of the amorphous solid is determined by two contributions. The dissolution inside the considered pores and the dissolution caused by other effects, e.g. by dissolution in other pores, or on the outer surface area of the amorphous gel particles. Under the assumption that the amount which gets dissolved in the considered pores is much smaller than the overall dissolved amorphous solid the source term in the population balance Eq. (A.1) can be expressed as:

$$\Gamma(t,\varsigma) = -k_H(C_{sol} - C_{eq,am})\varsigma \tag{A.5}$$

Since the density of the equally distributed pores gets lower by the same amount as the reaction medium itself. The resulting population balance equation is given by Eq. (A.6).

$$\partial_t \varsigma(t,r) + k_S(C_{sol} - C_{eq,am})\partial_r \varsigma(t,r) = -k_H(C_{sol} - C_{eq,am})\varsigma(t,r) \tag{A.6}$$

This equation can be solved using the method of moments. The zeroth moment represents the overall pore length $L_E(t)$. The inner surface area S can be computed from the first moment.

$$L_E = \int_0^\infty \varsigma(t,r)dr \tag{A.7}$$

$$S = 2\pi\int_0^\infty r\varsigma(t,r)dr \tag{A.8}$$

The application of the integral transform to the population balance Eq. (A.6) gives the following ODE description:

$$\partial_t L_E = -k_H(C_{sol} - C_{eq,am})L_E(t) \tag{A.9}$$

$$\partial_t S = 2\pi k_S(C_{sol} - C_{eq,am})L_E(t) - k_H(C_{sol} - C_{eq,am})S(t) \tag{A.10}$$

It can be seen that the linear differential Eq. (A.9) of the overall length L_E is analogous to the governing equation of the evolution of the amorphous solid $C_{am}(t)$. Therefore, the following statement is valid:

$$L_\varsigma(t) = K_L C_{am}(t). \tag{A.11}$$

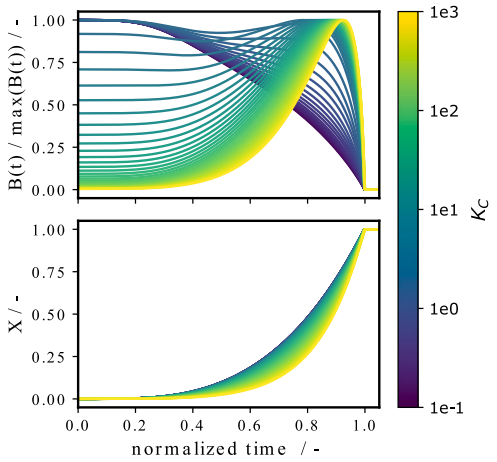

Fig. A.14. Effect of the constant K_C on the nucleation rate $B(t)$ and evolution of the crystallinity.

Using (A.11), the differential equation of the total surface $S(t)$ can be reformulated in the following way:

$$\partial_t S(t) = 2\pi k_S (C_{sol} - C_{eq,am}) K_L C_{am}(t) - k_H (C_{sol} - C_{eq,am}) S(t) \quad \text{(A.12)}$$

$$= (C_{sol} - C_{eq,am})(2\pi k_S K_L C_{am}(t) - k_H S(t)) \quad \text{(A.13)}$$

$$= k_H (C_{sol} - C_{eq,am})(2\pi k_S K_L k_H^{-1} C_{am}(t) - S(t)) \quad \text{(A.14)}$$

$$= k_H (C_{sol} - C_{eq,am})(K_C C_{am}(t) - S(t)). \quad \text{(A.15)}$$

If the temperature dependencies of k_S and k_H are the same, this results in a temperature independent constant K_C.

A.2. Effect of the surface evolution on the crystal growth

The effect of the constant K_C on the nucleation rate and the evolution of the crystallinity is shown in Fig. A.14. The nucleation rate is normalized to the maximal nucleation rate over time and time is normalized to the time to reach full crystallinity. For low values of K_C, the nucleation is similar to heterogeneous nucleation. The nucleation rate has the maximum at the beginning of the reaction since there the amorphous solid amount is maximal. With a higher value of K_C, the nucleation profile changes, the maximum of the nucleation rate is shifted towards the end of the crystallization process, which is similar to an autocatalytic nucleation mechanism. The curvature of the crystallinity increases with higher values of K_C.

Appendix B. Dynamic model

B.1. Thermal model

To describe the thermal behavior of the process the partial differential equation system based on the Eqs. (3),(4), (5) has to be solved. The parameters of these equations are given in Table B.3.

B.2. Kinetic model

The kinetic model of the process has to be solved together with the thermal model or sequentially, with the knowledge of the temperature field. The convection diffusion partial differential equation system stated by Eq. (1) has to be solved, with the scaled reaction terms.

The concentration of the amorphous solid $C_{am,abs}$ and the concentration of the dissolved solid $C_{sol,abs}$ are scaled with the total solid concentration $C_{total,abs}$ to calculate the scaled concentration of the amorphous solid $C_{am,s}$ and the scaled concentration of the dissolved solid $C_{sol,s}$.

$$C_{am,s} = C_{am,abs}/C_{total} \quad \text{(B.1)}$$

$$C_{sol,s} = C_{sol,abs}/C_{total} \quad \text{(B.2)}$$

The moments $\mu_{k,abs}$ are scaled with the factor $\pi/6v_m$ and the total solid concentration. Furthermore, the moments are scaled with the length l_{ref} of 1 µm, to obtain the scaled moments $\mu_{k,s}$

$$\mu_{3,s} = \frac{6v_m}{\pi C_{total}} \mu_{3,abs} \quad \text{(B.3)}$$

$$\mu_{2,s} = \frac{6v_m}{\pi C_{total}} l_{ref}^1 \mu_{2,abs} \quad \text{(B.4)}$$

$$\mu_{1,s} = \frac{6v_m}{\pi C_{total}} l_{ref}^2 \mu_{1,abs} \quad \text{(B.5)}$$

$$\mu_{0,s} = \frac{6v_m}{\pi C_{total}} l_{ref}^3 \mu_{0,abs}. \quad \text{(B.6)}$$

From this follows that the scaled third moment is equal to the scaled zeolite concentration ($C_{zeo,s} = \mu_{3,s}$). The scaled reaction terms are shown below, in these only the scaled concentrations and moments are used.

$$H(t,z) = k_{H,0} \exp\left(\frac{E_{A,H}}{R \cdot T_R}\right) \cdot (C_{sol} - C_{eq,am}) \cdot C_{am} \quad \text{(B.7a)}$$

$$G(t,z) = k_{g,0} \exp\left(\frac{E_{A,g}}{R \cdot T_R}\right) \cdot (C_{sol} - C_{eq,zeo}) \quad \text{(B.7b)}$$

$$B(t,z) = k_{B,0} \exp\left(\frac{E_{A,B}}{R \cdot T_R}\right) \cdot S \cdot (C_{sol} - C_{eq,zeo}) \quad \text{(B.7c)}$$

$$\kappa_{C_{am}}(t,z) = -H(t,z) \quad \text{(B.7d)}$$

$$\kappa_{C_{sol}}(t,z) = H(t,z) - \kappa_{\mu_3}(t,z) \quad \text{(B.7e)}$$

$$\kappa_S(t,z) = k_H \cdot (C_{eq,am} - C_{sol}) \cdot (K_C C_{am} - S) \quad \text{(B.7f)}$$

$$\kappa_{\mu_0}(t,z) = B(t,z) \quad \text{(B.7g)}$$

$$\kappa_{\mu_1}(t,z) = G(t,z) \cdot \mu_0 \quad \text{(B.7h)}$$

$$\kappa_{\mu_2}(t,z) = 2 \cdot G(t,z) \cdot \mu_1 \quad \text{(B.7i)}$$

$$\kappa_{\mu_3}(t,z) = 3 \cdot G(t,z) \cdot \mu_2 \quad \text{(B.7j)}$$

The required scaled parameters and inlet conditions are given in Table B.4

Table B.3
Parameters of the thermal model.

Name	Value	Unit
$z_{heater,1,begin}$	0	m
$z_{heater,1,end}$	14.4	m
$z_{heater,2,begin}$	14.4	m
$z_{heater,2,end}$	38.4	m
$z_{heater,3,begin}$	38.4	m
$z_{heater,3,end}$	42.4	m
L	42.4	m
$\rho_R A_R$	1.595	kg m^{-1}
$\rho_R c_{p,R} A_R$	5836.97	J K^{-1} m^{-1}
$\rho_w c_{p,w} A_w$	4550.53	J K^{-1} m^{-1}
$\rho_J c_{p,J} A_J$	2452.68	J K^{-1} m^{-1}
$\lambda_w/\rho_w c_{p,w}$	3.75e−6	s^{-1}
$kA_{R,w}$	228.673	J s^{-1} K^{-1}
$kA_{R,w,end}$	983.122	J s^{-1} K^{-1}
$kA_{w,J}$	362.86	J s^{-1} K^{-1}
$kA_{E,J}$	2.111	J s^{-1} K^{-1}
$v_{oil,i}$	0.15	m s^{-1}
T_E	293.15	K

Table B.4
Parameters of the kinetic model.

Name	Value	Unit
L	42.4	m
S_{in}	1	–
$C_{am,in}$	0.9547	–
$C_{sol,in}$	0.0453	–
$\mu_{0,in}$	0	–
$\mu_{1,in}$	0	–
$\mu_{2,in}$	0	–
$\mu_{3,in}$	0	–
$k_{H,0}$	4.469e6	s^{-1}
$E_{A,H}$	14 740	J mol^{-1}
$k_{B,0}$	3.351e9	s^{-1}
$E_{A,B}$	78 324	J mol^{-1}
K_c	0.00345	–
$k_{g,0}$	2.493e9	s^{-1}
$E_{A,g}$	78 324	J mol^{-1}
$C_{eq,am}$	0.0453	–
$C_{eq,zeo}$	0.025	–
$\rho_R A_R$	1.595	kg m^{-1}
Pe	240.2	–

References

[1] C.S. Cundy, P.A. Cox, The hydrothermal synthesis of zeolites: Precursors, intermediates and reaction mechanism, Microporous Mesop. Mater. 82 (2005) 1–78, http://dx.doi.org/10.1016/j.micromeso.2005.02.016.

[2] H. Toufar, Technische und ökonomische Aspekte industrieller Zeolithsynthesen, Chem. Ing. Tech. 82 (2010) 1049–1058, http://dx.doi.org/10.1002/cite.201000073.

[3] A.-N. Parvulescu, S. Maurer, Toward sustainability in zeolite manufacturing: An industry perspective, Front. Chem. 10 (2022) 1050363, http://dx.doi.org/10.3389/fchem.2022.1050363.

[4] M.B. Plutschack, B. Pieber, K. Gilmore, P.H. Seeberger, The Hitchhiker's guide to flow chemistry, Chem. Rev. 117 (2017) 11796–11893, http://dx.doi.org/10.1021/acs.chemrev.7b00183.

[5] Z. Liu, J. Zhu, C. Peng, T. Wakihara, T. Okubo, Continuous flow synthesis of ordered porous materials: From zeolites to metal–organic frameworks and mesoporous silica, React. Chem. Eng. 4 (2019) 1699–1720, http://dx.doi.org/10.1039/C9RE00142E.

[6] N.A. Azri, R. Patel, G. Ozbuyukkaya, C. Kowall, G. Cormack, N. Proust, R. Enick, G. Veser, Batch-to-continuous transition in the specialty chemicals industry: Impact of operational differences on the production of dispersants, Chem. Eng. J. 445 (2022) 136775, http://dx.doi.org/10.1016/j.cej.2022.136775.

[7] A. Deneyer, Q. Ke, J. Devos, M. Dusselier, Zeolite synthesis under nonconventional conditions: Reagents, reactors, and *Modi Operandi*, Chem. Mater. 32 (2020) 4884–4919, http://dx.doi.org/10.1021/acs.chemmater.9b04741.

[8] C. Cundy, M. Henty, R. Plaisted, Zeolite synthesis using a semicontinuous reactor, part 1: Controlled nucleation and growth of ZSM-5 crystals having well-defined morphologies, Zeolites 15 (1995) 353–372, http://dx.doi.org/10.1016/0144-2449(94)00052-T.

[9] Z. Liu, T. Wakihara, C. Anand, S.H. Keoh, D. Nishioka, Y. Hotta, T. Matsuo, T. Takewaki, T. Okubo, Ultrafast synthesis of silicalite-1 using a tubular reactor with a feature of rapid heating, Microporous Mesop. Mater. 223 (2016) 140–144, http://dx.doi.org/10.1016/j.micromeso.2015.11.001.

[10] T. Vandermeersch, T.R. Va. Assche, J.F. Denayer, W.D. Malsche, A continuous flow reactor setup as a tool for rapid synthesis of micron sized NaA zeolite, Microporous Mesop. Mater. 226 (2016) 133–139, http://dx.doi.org/10.1016/j.micromeso.2015.12.039.

[11] M. Mackley, X. Ni, Mixing and dispersion in a baffled tube for steady laminar and pulsatile flow, Chem. Eng. Sci. 46 (1991) 3139–3151, http://dx.doi.org/10.1016/0009-2509(91)85017-R.

[12] M. Mackley, P. Stonestreet, Heat transfer and associated energy dissipation for oscillatory flow in baffled tubes, Chem. Eng. Sci. 50 (1995) 2211–2224, http://dx.doi.org/10.1016/0009-2509(95)00088-M.

[13] S. Lawton, G. Steele, P. Shering, L. Zhao, I. Laird, X.-W. Ni, Continuous crystallization of pharmaceuticals using a continuous oscillatory baffled crystallizer, Org. Process Res. Dev. 13 (2009) 1357–1363, http://dx.doi.org/10.1021/op900237x.

[14] X. Ni, A. Liao, Effects of mixing, seeding, material of baffles and final temperature on solution crystallization of l-glutamic acid in an oscillatory baffled crystallizer, Chem. Eng. J. 156 (2010) 226–233, http://dx.doi.org/10.1016/j.cej.2009.10.045.

[15] N. Masngut, A.P. Harvey, J. Ikwebe, Potential uses of oscillatory baffled reactors for biofuel production, Biofuels 1 (2010) 605–619, http://dx.doi.org/10.4155/bfs.10.38.

[16] S. Nicolas, C. Lutz, J.-L. Dubois, Y. Lecomte, Method for the continuous synthesis of zeolite crystals, 2018.

[17] H. Ramire. Mendoza, M. Valdez, T. van Gerven, C. Lutz, Continuous flow synthesis of zeolite FAU in an oscillatory baffled reactor, J. Adv. Manuf. Process. 2 (2020) http://dx.doi.org/10.1002/amp2.10038.

[18] H. Toufar, K.-P. Wendlandt, H.G. Karge, A simple model for the kinetic evaluation of zeolite crystallization processes, J. Chem. Soc., Faraday Trans. 91 (1995) 549, http://dx.doi.org/10.1039/ft9959100549.

[19] M. Avrami, Kinetics of phase change. II transformation-time relations for random distribution of nuclei, J. Chem. Phys. 8 (1940) 212–224, http://dx.doi.org/10.1063/1.1750631.

[20] A.F. Gualtieri, Synthesis of sodium zeolites from a natural halloysite, Phys. Chem. Miner. 28 (2001) 719–728, http://dx.doi.org/10.1007/s002690100197.

[21] R.W. Thompson, A. Dyer, A modified population balance model for hydrothermal molecular sieve zeolite synthesis, Zeolites 5 (1985) 292–301, http://dx.doi.org/10.1016/0144-2449(85)90161-7.

[22] V. Nikolakis, D.G. Vlacho, M. Tsapatsis, Modeling of zeolite crystallization: The role of gel microstructure, Microporous Mesop. Mater. 21 (1998) 337–346, http://dx.doi.org/10.1016/S1387-1811(98)00017-1.

[23] B. Houska, F. Logist, J. Va. Impe, M. Diehl, Robust optimization of nonlinear dynamic systems with application to a jacketed tubular reactor, J. Process Control 22 (2012) 1152–1160, http://dx.doi.org/10.1016/j.jprocont.2012.03.008.

[24] J. Luedtke, S. Ahmed, A sample approximation approach for optimization with probabilistic constraints, SIAM J. Optim. 19 (2008) 674–699, http://dx.doi.org/10.1137/070702928.

[25] S. Julier, J. Uhlmann, H. Durrant-Whyte, A new approach for filtering nonlinear systems, in: Proceedings of 1995 American Control Conference, vol. 3, ACC'95, American Autom Control Council, Seattle, WA, USA, 1995, pp. 1628–1632, http://dx.doi.org/10.1109/ACC.1995.529783.

[26] S. Recker, P. Kühl, M. Diehl, H.G. Bock, Sigmapoint approach for robust optimization of nonlinear dynamic systems, in: International Conference on Simulation and Modeling Methodologies, Technologies and Applications, 2018.

[27] R. Semrau, S. Engell, Process as a battery: Electricity price aware optimal operation of zeolite crystallization in a continuous oscillatory baffled reactor, Comput. Chem. Eng. (2023) 108143, http://dx.doi.org/10.1016/j.compchemeng.2023.108143.

[28] A. Julbe, M. Drobek, Zeolite X: Type, in: E. Drioli, L. Giorno (Eds.), Encyclopedia of Membranes, Springer Berlin Heidelberg, Berlin, Heidelberg, 2014, pp. 1–2, http://dx.doi.org/10.1007/978-3-642-40872-4_607-1.

[29] H. Ramire Mendoza, Ultrasound-Assisted Synthesis of Zeolite Catalysts (Ph.D. thesis), KU Leuven, 2020.

[30] M. Manninen, E. Gorshkova, K. Immonen, X.-W. Ni, Evaluation of axial dispersion and mixing performance in oscillatory baffled reactors using CFD: Axial dispersion and mixing performance in oscillatory baffled reactors, J. Chem. Technol. Biotechnol. 88 (2013) 553–562, http://dx.doi.org/10.1002/jctb.3979.

[31] O. Levenspiel, The Chemical Reactor Omnibook, veränd. u. korr. neuausg. ed., lulu.com, Raleigh, NC, 2013.

[32] S. Yang, A. Navrotsky, B.L. Phillips, An in situ calorimetric study of the synthesis of FAU zeolite, Microporous Mesop. Mater. 46 (2001) 137–151, http://dx.doi.org/10.1016/S1387-1811(01)00268-2.

[33] R.W. Thompson, A. Dyer, Mathematical analyses of zeolite crystallization, Zeolites 5 (1985) 202–210, http://dx.doi.org/10.1016/0144-2449(85)90086-7.

[34] S.K. Bhatia, D.D. Perlmutter, A random pore model for fluid-solid reactions: I. Isothermal, kinetic control, AIChE J. 26 (1980) 379–386, http://dx.doi.org/10.1002/aic.690260308.

[35] G.T. Kerr, Chemistry of crystalline aluminosilicates. I. Factors affecting the formation of zeolite A, J. Phys. Chem. 70 (1966) 1047–1050, http://dx.doi.org/10.1021/j100876a015.

[36] T. Antonic, A. Ci, Dissolution of amorphous aluminosilicate zeolite precursors in alkaline solutions, J. Chem. Soc. Faraday Trans. 90 (1994) 4.

[37] B. Subotić, J. Bronić, T. Antoni´ Jelić, Theoretical and practical aspects of zeolite nucleation, in: Ordered Porous Solids, Elsevier, 2009, pp. 127–185, http://dx.doi.org/10.1016/B978-0-444-53189-6.00006-8.

[38] A. Palčić, B. Subotić, V. Valtchev, J. Bronić, Nucleation and crystal growth of zeolite a synthesised from hydrogels of different density, CrystEngComm 15 (2013) 5784, http://dx.doi.org/10.1039/c3ce40450.

[39] S. Gonthier, L. Gora, I. Güray, R.W. Thompson, Further comments on the role of autocatalytic nucleation in hydrothermal zeolite syntheses, Zeolites 13 (1993) 414–418, http://dx.doi.org/10.1016/0144-2449(93)90113-H.

[40] B. Subotić, T. Antonić, Lnfluence of physicochemical and structural properties of aluminosilicate gel precursors on the kinetics of crystallization zeolites A and X, in: Proceedings of the 12th International Zeolite Conference, 1999.

[41] H. Lechert, H. Kacirek, The kinetics of nucleation of X zeolites, Zeolites 13 (1993) 192–200, http://dx.doi.org/10.1016/S0144-2449(05)80277-5.

[42] A.E. Bouaswaig, S. Engell, WENO scheme with static grid adaptation for tracking steep moving fronts, Chem. Eng. Sci. 64 (2009) 3214–3226, http://dx.doi.org/10.1016/j.ces.2009.03.040.

[43] F. Acker, R.B. de R. Borges, B. Costa, An improved WENO-Z scheme, J. Comput. Phys. 313 (2016) 726–753, http://dx.doi.org/10.1016/j.jcp.2016.01.038.

[44] J.A.E. Andersson, J. Gillis, G. Horn, J.B. Rawlings, M. Diehl, CasADi: A software framework for nonlinear optimization and optimal control, Math. Program. Comput. 11 (2019) 1–36, http://dx.doi.org/10.1007/s12532-018-0139-4.

[45] A.C. Hindmarsh, P.N. Brown, K.E. Grant, S.L. Lee, R. Serban, D.E. Shumaker, C.S. Woodward, SUNDIALS: Suite of nonlinear and differential/algebraic equation solvers, ACM Trans. Math. Software 31 (2005) 363–396, http://dx.doi.org/10.1145/1089014.1089020.

[46] F. Gao, L. Han, Implementing the Nelder-Mead simplex algorithm with adaptive parameters, Comput. Optim. Appl. 51 (2012) 259–277, http://dx.doi.org/10.1007/s10589-010-9329-3.

[47] R.R. Rhinehart, Nonlinear Regression Modeling for Engineering Applications: Modeling, Model Validation, and Enabling Design of Experiments, first ed., Wiley, 2016, http://dx.doi.org/10.1002/9781118597972.

[48] K. Smith, M. Mackley, An experimental investigation into the scale-up of oscillatory flow mixing in baffled tubes, Chem. Eng. Res. Des. 84 (2006) 1001–1011, http://dx.doi.org/10.1205/cherd.05054.

[49] K.B. Smith, Scale-Up of Oscillatory Flow Mixing, (Ph.D. thesis), Christ's College, Cambridge, 2000.

[50] S. Yang, A. Navrotsky, An in situ calorimetric study of zeolite crystallization kinetics, Microporous Mesop. Mater. 52 (2002) 93–103, http://dx.doi.org/10.1016/S1387-1811(02)00276-7.

[51] A. Wächter, L.T. Biegler, On the implementation of an interior-point filter line-search algorithm for large-scale nonlinear programming, Math. Program. 106 (2006) 25–57, http://dx.doi.org/10.1007/s10107-004-0559-y.

[52] I.S. Duff, J.K. Reid, The multifrontal solution of indefinite sparse symmetric linear, ACM Trans. Math. Software 9 (1983) 302–325, http://dx.doi.org/10.1145/356044.356047.

[53] M. Cegla, A. Buczko, S. Kemmerling, S. Engell, Experimental application of real-time optimization with modifier adaptation and quadratic approximation to a reactive extrusion process, IFAC-PapersOnLine 57 (2023).